Angle-dependent protrusion of cell membranes

Huayuan Tang [a,b], Hongfei Ye [b], Hongwu Zhang [b], Xin Yi [c,*], Yonggang Zheng [b,*]

[a] *Department of Engineering Mechanics, Hohai University, Nanjing 210098, PR China*
[b] *International Research Center for Computational Mechanics, State Key Laboratory of Structural Analysis for Industrial Equipment, Department of Engineering Mechanics, Faculty of Vehicle Engineering and Mechanics, Dalian University of Technology, Dalian 116024, PR China*
[c] *Department of Mechanics and Engineering Science, State Key Laboratory for Turbulence and Complex Systems, College of Engineering, Peking University, Beijing 100871, PR China*

ABSTRACT

Protrusion induced by cylindrical tubes against cell membranes plays essential roles in numerous biological processes, including filopodia growth, cellular packing or entry of one-dimensional nanomaterials, and indentation of cells by needle-like probes. Though the mechanical interaction between the cell membrane and a perpendicular tube has been widely investigated, little is known about how an inclined protruding tube interacts with the cell membrane. Here, we theoretically investigate the angle-dependent protrusion of cylindrical tubes against cell membranes. It is found that perpendicular protrusion is stabilized by the elastic deformation of cell membranes. Increasing the angle between the protrusion direction and perpendicular direction or increasing membrane tension leads to an increasing peak force for the membrane tubulation and increasing plateau resistive force for the maintenance of membrane tubules. Moreover, two fundamental protruding modes leading to the tip-roof and finial-roof system configurations are identified. Inclined protrusion retards the configurational transition from the tip-roof to the finial-roof configuration, and causes possible bending and buckling of protruding tubes due to a large membrane resistive force. Our results offer fundamental insights into the interaction between cell membranes and one-dimensional nanomaterials, and contribute to the understanding and control of membrane protrusion in biological systems.

1. Introduction

The mechanical interplay between cell membranes and one-dimensional nanomaterials is ubiquitous in biological activities and strongly affects morphologies and functions of cells. For example, it is reported that carbon nanotubes, asbestos fibers, and gold nanowires adopt a perpendicular entry into living cells through a tip recognition and body rotation mechanism (Shi et al., 2011). Further theoretical investigations indicate that membrane wrapping of one-dimensional nanomaterials is dominated by normalized membrane tension with a perpendicular entry prevailing at small membrane tension and parallel adhering at a large membrane tension (Yi et al., 2014). The mutual interaction between vesicles and encapsulated of flexible filaments, such as nucleoid DNAs, actin filaments, and microtubules, results in the shaping of vesicles to dumpling-, sausage-, pebble-, droplet-, or racket-like morphologies (Shi et al., 2023). The adhesive interaction between lipid membranes and adsorbed nanoparticles could lead to cooperative wrapping of multiple nanoparticles in long tubular membrane structures enclosing nanoparticle chains (Raatz et al., 2014; Yue et al., 2014; Raatz

---

and Weikl, 2017; Wu and Yi, 2020).

Among different modes of interaction between cell membranes and one-dimensional nanomaterials, protrusion of cell membranes is widely encountered. Long and stiff carbon nanotubes shape the confining intracellular vesicles to a configuration with long membrane protrusions or protruding tips, and lead to length- and stiffness-dependent cytotoxicity (Zhu et al., 2016). Streaming tubular protrusions are observed in active nematic vesicles encapsulating microtubules and molecular motors (Keber et al., 2014). The formation of filopodia, vital for cellular sensing of the local environment, cell motility, and cell–cell communications, is driven by the protrusion of actin filament bundles against cell membranes via polymerization (Mattila and Lappalainen, 2008; Jacquemet et al., 2015; Chang et al., 2022). The initiation, maintenance, and retraction of the filopodia can be viewed as a mechanical interplay between one-dimensional actin filament bundles and cell membranes (Mogilner and Rubinstein, 2005; Atilgan et al., 2006). An interesting phenomenon is that one-dimensional nanomaterials usually protrude perpendicularly from cell membranes. For instance, filopodia grow perpendicularly with respect to the membrane edge with the actin filaments enclosed by a membrane tube (Atilgan et al., 2006; Liu et al., 2008). Experimental studies show that during spread the infecting rod-shaped bacterial parasite *Listeria monocytogenes* with a long actin tail protrudes against the cell membrane more or less perpendicularly (Tilney and Portnoy, 1989). However, fundamental questions about why the perpendicular protrusion is dominant in biological systems and how the tube protrusion angle regulates the interaction remain unanswered.

So far most theoretical works on the cellular interaction with one-dimensional nanomaterials are restricted to cases in which one-dimensional nanomaterials protrude against cell membranes perpendicularly due to axisymmetric system advantage (Mogilner and Rubinstein, 2005; Atilgan et al., 2006; He and Ji, 2017). The mechanical interaction of an inclined tube with the cell membrane, which is of more general significance, has rarely been explored theoretically due to the lack of high symmetry of the tube–membrane configuration. A general continuum model capable of revealing the role of tube protrusion direction is called for at a fundamental level and can provide implications in the protrusion angle-dependent biological activities. For instance, the filopodia sweep with the tip rotating around the fixed base to explore a larger space while sensing the local environment (Zidovska and Sackmann, 2011; Leijnse et al., 2015). Inclined microindentation, a versatile and unobstructive tool to explore cell mechanical properties, exerts controllable compressive nanonewton forces on cells with the indenter approaching the cells with a inclined angle (Gonzalez-Rodriguez et al., 2016). In this work, the protrusion of an inclined tube against the lipid membrane is investigated. It is found that the perpendicular protrusion is always accompanied by a minimal membrane deformation energy and suffers a minimal resistive force, suggesting the perpendicular protrusion is stabilized by the elastic deformation of the lipid membrane. Two characteristic configurations are identified and the effects of the protrusion angle, protrusion depth, and membrane tension on the force–protrusion depth relation and configurational transition are investigated. Analytical predictions on the resistive force and the membrane profile are provided. Implications of our results on biological processes, such as filopodial orientation, invasion of the rod-shaped bacteria, and instability of confined filaments, are discussed.

2. Theoretical modeling and numerical methods

2.1. Theoretical modeling

Consider a rigid cylindrical tube of radius R protruding against an initially flat cell membrane patch of radius ρ_{mem} at a protrusion angle θ (Fig. 1a). There is no adhesive interaction between the tube and membrane, and the size of the membrane patch is significantly larger than the tube radius ($\rho_{mem} = 500R$). A Cartesian coordinate system is adopted with the tube axis in the xz plane and the remote boundary of the membrane at $z = 0$. The protrusion depth h is defined as the z-coordinate of the tube tip. According to the Canham–Helfrich theory (Helfrich, 1973), the elastic energy E_{el} of the deformed membrane is

$$E_{el} = 2\kappa \int M^2 dA + \sigma \Delta A \tag{1}$$
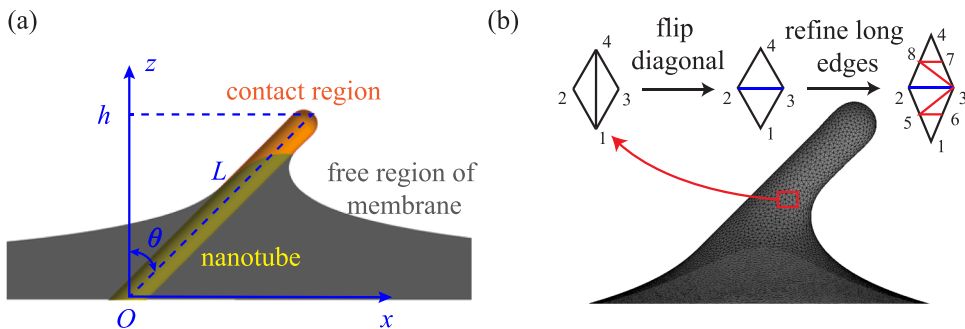
Fig. 1. (a) Schematic plot of a rigid tube protruding against a lipid membrane at a protrusion angle θ and protrusion depth h. The yellow part represents the tube, and the orange and gray parts denote the contact region and free region of the membrane, respectively. (b) The triangulated mesh of the membrane. Steps of improving mesh quality by flipping diagonals and refining long edges are shown on the top panel in (b).

where κ is the membrane bending rigidity and M is the mean curvature of the membrane surface. On the right-hand side of Eq. (1), the first term accounts for the membrane bending energy E_b and the second term describes the tension energy E_t with σ as the membrane tension and ΔA representing the excess membrane area induced by the protrusion. A short-ranged hard-core repulsive interaction U_{rep} between the membrane and tube is applied to avoid possible penetration between the membrane and tube, that is,

$$U_{rep} = \begin{cases} \dfrac{\epsilon}{3}\left[2\left(\dfrac{d_c}{d}\right)^{10} - 5\left(\dfrac{d_c}{d}\right)^4\right] + \epsilon, & d < d_c, \\ 0, & d \geq d_c. \end{cases} \tag{2}$$

Here d is the distance between the membrane and tube surface, d_c is a small cutoff distance only within which the repulsive potential exists, and ϵ is the strength of the repulsive interaction. In our simulations, $d_c = 0.05R$ and $\epsilon = 1$ are taken.

2.2. Numerical methods

To obtain the equilibrium system configuration at a given set (θ, h/R), the membrane surface is described as a triangulated surface using Surface Evolver (Brakke, 1992). The mean curvature M of the membrane surface at the triangle vertex i is given by

$$M = \frac{3\nabla A_i \cdot \nabla V_i}{2(\nabla A_i \cdot \nabla A_i)} \tag{3}$$

where A_i and V_i are the area and volume associated with vertex i, respectively, and ∇A_i and ∇V_i are the corresponding gradients at vertex i, which can be calculated based on the vertex coordinates. The volume associated with vertex i of n neighboring vertices can be calculated by
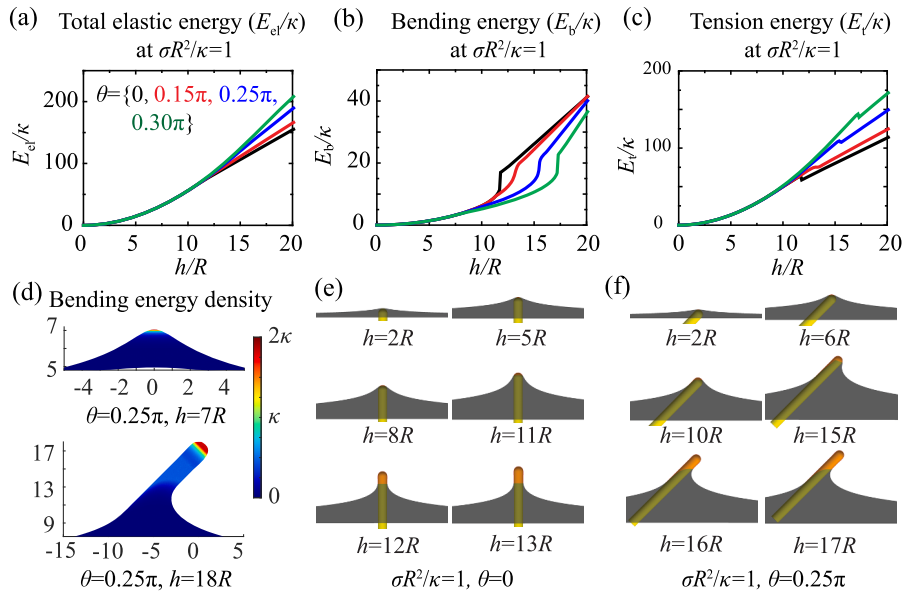
$$V_i = \frac{1}{6}\mathbf{r} \cdot (\mathbf{r}_1 \times \mathbf{r}_2 + \mathbf{r}_2 \times \mathbf{r}_3 + \cdots + \mathbf{r}_n \times \mathbf{r}_1) \tag{4}$$

where $\mathbf{r}$ is the position vector of vertex i and $\mathbf{r}_1$, $\mathbf{r}_2$, ..., $\mathbf{r}_n$ are the position vectors of the neighboring vertices. Thus, the gradient ∇V_i is

$$\nabla V_i = \frac{1}{6}(\mathbf{r}_1 \times \mathbf{r}_2 + \mathbf{r}_2 \times \mathbf{r}_3 + \cdots + \mathbf{r}_n \times \mathbf{r}_1) \tag{5}$$

For a triangulated membrane with N vertices, the bending energy is then given by

$$E_b = 2\kappa \sum_i^N \frac{A_i}{3} \cdot \left(\frac{3\nabla A_i \cdot \nabla V_i}{2\nabla A_i \cdot \nabla A_i}\right)^2 \tag{6}$$

Fig. 2. Variations of the total elastic energy E_{el} (a), membrane bending energy $E_b = 2\kappa \int M^2 dA$ (b), and membrane tension energy $E_t = \sigma \Delta A$ (c) as a function of the protrusion depth h at $\sigma R^2/\kappa = 1$ and different values of the protrusion angle θ. (d) The bending energy density $2\kappa M^2$ of the deformed membrane at $\sigma R^2/\kappa = 1$, $\theta = 0.25\pi$ and $h = 7R$ (top panel) and $h = 18R$ (bottom panel). (e, f) Configurational evolution for $\sigma R^2/\kappa = 1$ with increasing protrusion depth h at $\theta = 0$ (e) and 0.25π (f).

The equilibrium configuration at a given protrusion depth is obtained by minimizing the total energy of the tube–membrane system with respect to the vertex coordinates. A combination of the gradient descent, conjugate gradient, and Hessian methods is employed to minimize the total energy until the relative energy change between two minimization steps is less than (1×10^{-6}) κ. To mimic the protrusion process, we gradually increase the protrusion depth h with a small increment Δh starting from a flat membrane ($h = 0$). In our calculations, a sufficiently small value of $\Delta h = 0.1R$ is taken to capture configurational transitions. Having knowledge of $E_{el}(h)$, the resistive force inhibits the perpendicular motion of the enclosed tube can be determined as $f(h) = dE_{el}/dh$.

The triangulated mesh can be severely deformed as the protrusion depth increases, especially in the contact region between the membrane and tube, reducing the numerical accuracy. To address this issue, the triangulated membrane is remeshed every few minimization steps to ensure the size of each triangle edge l falling in a range $l_{min} < l < l_{max}$ by flipping diagonals and refining long edges (Fig. 1b). In our simulations we set $l_{max} = 0.01R$ and $l_{min} = 0.002R$ to ensure the fine description of the membrane at an affordable computational cost. Specifically, each edge is examined with respect to the angles of the quadrilateral formed by two adjoining triangles. If the summation of the opposite angles off the diagonal is larger than π (e.g., $\angle 124 + \angle 134 > \pi$ in Fig. 1b), the diagonal is switched to form a new pair of triangles. As the interested triangles further elongate, flipping the diagonals alone does not lead to an improvement in the equiangulation, and new vertices are introduced in the middle of the edge with a length longer than l_{max} (e.g., vertices 7 and 8 are added in the middle of lines 3-4 and 2-4, respectively, in Fig. 1b). No subdivision is performed for the edge with a length shorter than $2l_{min}$ (e.g., line 2-3 in Fig. 1b). Then, these new added vertices are connected to form new triangles. The flipping diagonal and refining procedures are repeated several times over the whole membrane surface to improve the mesh quality.

3. Numerical and theoretical results

3.1. Elastic deformation energy

Profiles of the total elastic energy E_{el}/κ of the membrane and its two components E_b and E_t versus the normalized protrusion depth h /R at $\sigma R^2/\kappa = 1$ and different values of the protrusion angle θ are shown in Fig. 2a–c. E_{el}/κ increases with increasing θ at a given h/R, indicating that the perpendicular protrusion mode is energetically favorable. Experiments show that the membrane tubule formed on the axon is perpendicular to the membrane surface, and the tubule becomes inclined by applying a lateral displacement on the tubule tip while the tubule would later slide back to maintain the perpendicular orientation (Datar et al., 2015), consistent with our results that the perpendicular protrusion is more energetically stable over inclined protrusion. The profile $E_{el}(h)$ shows cubic nonlinearity at relatively small protrusion depth but a linear feature at large protrusion depth (Fig. 2a). The difference in order corresponds to kinks in the profile $E_{el}(h)$, which result from discontinuities in profiles of $E_b(h)$ and $E_t(h)$ (Fig. 2a–c), signifying discontinuous configurational transition (Fig. 2d–f). The clarity of the appearance of the energy kinks in $E_{el}(h)$ hinges on the disparity between the energy jumps in E_b and the energy drops in E_t. Magnitudes of the energy jumps in Fig. 2b and energy drops in Fig. 2c are quite similar, resulting in unclear kinks in Fig. 2a.

3.2. Configurational transitions during the protrusion

As demonstrated in Fig. 2e,f for the evolution of equilibrium configurations with increasing protrusion depth h /R for σR^2 /$\kappa = 1$ at θ=0 and 0.25π, two distinct configurations can be identified. At a small value of the protrusion depth h, the membrane forms contact with a part of the spherical tube cap and a very small part of the tube wall (Fig. 2d). The inner membrane having contact with the tube forms a protruding tip and the outer free membrane undergoing small deformation adopts a catenoidal roof-like shape with very small mean curvature, as indicated by the low bending energy density in Fig. 2d. Therefore, the membrane configuration at small h is referred to as the tip-roof configuration, and no membrane overhangs exist. At a large protrusion depth, the tube tip is fully covered by the membrane and membrane overhangs could occur for an inclined protruding tube. As h further increases, a clear finial-like tubular membrane protrusion forms. Therefore, the membrane configuration at large h is referred to as the finial-roof configuration. Fig. 2b,c indicates that both E_b and E_t increase nonlinearly with increasing h/R for the tip-roof configuration and they further increase linearly with increasing h/R for the finial-roof configuration, suggesting that the energy variation for the finial-roof configuration mainly arises
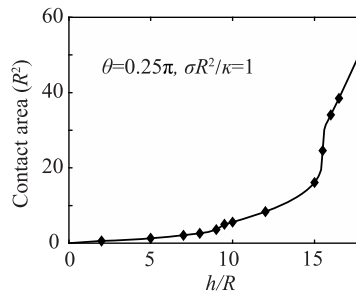

Fig. 3. Contact area between the membrane and tube versus the protrusion depth at the protrusion angle $\theta = 0.25\pi$ and membrane tension σR^2 /κ $= 1$.

from the membrane tubule elongation with constant bending and tension energy per axial length. Moreover, the membrane tension energy E_t exceeds the bending energy E_b during the tube protrusion (Fig. 2b,c with $\sigma R^2/\kappa = 1$), together with the variation of slopes dE_b/dh and dE_t/dh, indicating that the tension dominates in the outer region of the membrane and the bending deformation becomes increasingly important in the inner membrane region. Upon the transition from the tip-roof configuration to the finial-roof configuration, the slope dE_t/dh becomes smaller (Fig. 2c), indicating that the configurational transition results in a decrease in the membrane area. One can then deduce that a larger membrane tension favors the configurational transition at a smaller protrusion depth.

3.3. Evolution of the tube–membrane contact region

To gain a more detailed understanding of the protrusion process, we evaluate the contact area between the membrane and tube as a function of the protrusion depth with $\theta = 0.25\pi$ and $\sigma R^2/\kappa = 1$ (Fig. 3), and contact morphologies corresponding to diamond symbols in Fig. 3 are shown in Fig. 4. The evolution of the contact area and contact morphologies at $\theta = 0$ and $\sigma R^2/\kappa = 1$ are shown in Figs. S1 and S2 for comparison. At a small protrusion depth (e.g., h=2R, 5R, 7R, and 8R), the membrane interacts with the spherical cap of the tube. The contact lines are circles parallel to the x-y plane and the base radii of the cap gradually increase with the protrusion depth. As the protrusion depth h further increases (e.g., h=9R, 9.5R, 10R, 12R, and 15R), the contact region extends to the tube wall region before the spherical tube cap is fully wrapped by the membrane. For the protrusion at an inclined angle, the upper region of the tube tends to contact with the membrane first and impede the membrane deformation. The contact region on the tube wall is of slender shape with the width gradually decreasing along the tube axis. In this stage, the length of the tube contact region increases with the protrusion depth, and the contact region on the spherical cap expends until the cap is fully wrapped (e.g., h=15.5R). After that, the membrane starts to shrink and forms a tubular structure near the hemispherical end contacting with the lower part of the tube (e.g., h=16R and 16.5R), resulting in a sharp increase of the contact area in Fig. 3. Further increase of the protrusion depth leads to the elongation of the tubular structure while the overall shape of contact region keeps unchanged, consistent with the linear increase of the contact area with the protrusion depth (Fig. 3). For the perpendicular protrusion (Fig. S1), the contact area first nonlinearly increases with the protrusion depth as the membrane contacts and fully wraps the spherical cap of the tube (Fig. S2). After that, the membrane forms a tubular structure enclosing the tube (Fig. S2), and the contact area increases linearly with the protrusion depth (Fig. S1). Overall, the evolution of the contact area can be divided into two stages. One stage is the nonlinear growth stage with the tube–membrane contact region expanding on the cap and upper part of the tube, followed by the other stage, a linear growth stage with the protrusion proceeding with the elongation of the tubular structure.
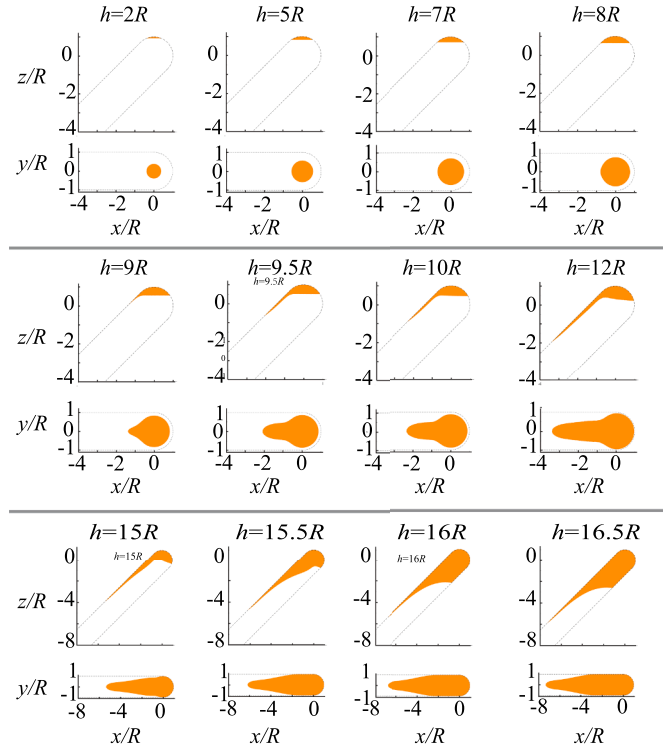

Fig. 4. Evolution of the tube–membrane contact region at various protrusion depths with $\theta = 0.25\pi$ and $\sigma R^2/\kappa = 1$. The contact regions (orange) are shown in the x-z (upper panels) and x-y (lower panels) views with the Cartesian coordinate of the tube cap center reset to be (0, 0, 0) for comparison.

For a free cylindrical membrane tubule of bending rigidity κ and tension σ, it has an equilibrium radius $r_0 = \sqrt{\kappa/(2\sigma)}$ (Derényi et al., 2002; Powers et al., 2002; Harmandaris and Deserno, 2006; Tian et al., 2018; Tang et al., 2019). Therefore, at small membrane tension of $\sigma R^2/\kappa < 1/2$, the radius of the tubular membrane protrusion adopts a radius of r_0, larger than the tube radius R. Fig. S3 demonstrates that, in this scenario of a small membrane tension, a transition occurs from the tip-roof to the finial-roof configuration, resulting in the formation of a membrane tubule of radius $r_0 > R$ as the protrusion depth increases. Furthermore, a more detailed examination of the configurations in Fig. S3, when coupled with measurements of the contact area shown in Figs. S4 and S5, indicates that the membrane tubule primarily makes contact with the upper portion of the enclosed tube, even in the finial-roof configuration. This leads to substantial gaps between the membrane and the lower part of the tube, in contrast to the tight contact observed between the tubule and the enclosed tube at higher membrane tension.

3.4. Configurational transitions regulated by the membrane tension

To further demonstrate the role of the membrane tension on the configurational evolution of the system, comparisons between system configurations at the same protrusion depth h but different values of membrane tension $\sigma R^2/\kappa$ are conducted. Case studies at $h = 15R$ and $\theta = 0.25\pi$ show that the tip-roof configuration prevails at a lower membrane tension and the finial-roof configuration prevails at a higher membrane tension (Fig. 5a). As the tension energy is linearly proportional to the area excess of the membrane, the variation of the slope dE_t/dh around the profile discontinuities in Fig. 2c suggests that the finial-roof configuration saves the membrane area in comparison with the tip-roof configuration. Since the membrane deformation is dominated by the membrane tension of a finite value, the transition from the tip-roof configuration to the finial-roof configuration is expected as the membrane tension increases, releasing the tension energy with compensation of increasing bending energy induced by the membrane tubule covering the protruding tube.

The configurational transition governed by the competition between bending and tension energies is summarized in a protrusion phase diagram (Fig. 5b). In comparison with the finial-roof configuration, the tip-roof configuration is more energetically favorable at a smaller $\sigma R^2/\kappa$ and a larger protrusion angle θ. At a given θ, the critical membrane tension for the configurational transition decreases with increasing protrusion depth. Dependence of the dimensionless parameter $\sigma R^2/\kappa$ implies the size effect of the tube on the system configuration. As $\sigma R^2/\kappa$ is proportional to the tube radius R, a transition from the tip-roof to the finial-roof configuration is expected as R increases. The filopodia–membrane system adopts a typical finial-roof configuration and, according to our results, the finial-roof configuration is enhanced by the formation of actin filament bundles of a larger radius.

3.5. Resistive force during the protrusion

A successful tubular protrusion requires overcoming the resistive force f associated with the membrane deformation (Derényi et al., 2002; Powers et al., 2002; Koster et al., 2005; Jiang and Powers, 2008; Jiang, 2012; Tian et al., 2018; Tang et al., 2019; Zhang et al., 2022). Fig. 6a shows the normalized resistive force fR/κ as a function of the protrusion depth h/R at different values of the protrusion angle θ and membrane tension σ. In the early protrusion stage, the resistive force increases almost linearly with the protrusion depth and the system adopts the tip-roof configuration. Upon further protrusion f shows weakly nonlinear dependency on h/R before the resistive force rises to its peak value f_{max}. Then the resistive force drops and reaches a plateau after slight oscillation, corresponding to the formation and maintenance of a stable finial-roof configuration. The $f - h/R$ profile exhibits a nonmonotonic feature. Similar nonmonotonic force–displacement profiles were observed in the indentation of pore-spanning lipid membranes by cylindrical indenters (Zhang et al., 2022) and in the packing of long stiff nanorods in vesicles (Zhu et al., 2016; Zou et al., 2018), which is expected as the formation of a tubular membrane protrusion is a localized occurrence.

The presence of a peak resistive force, f_{max}, can be attributed to the geometry of the enclosed tube. Our previous studies
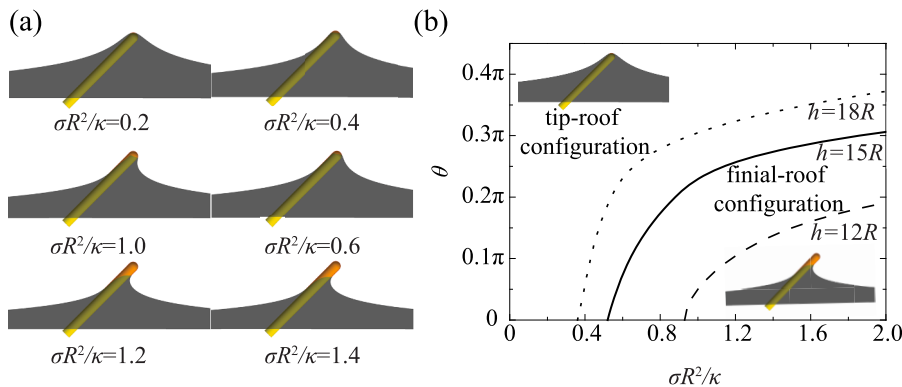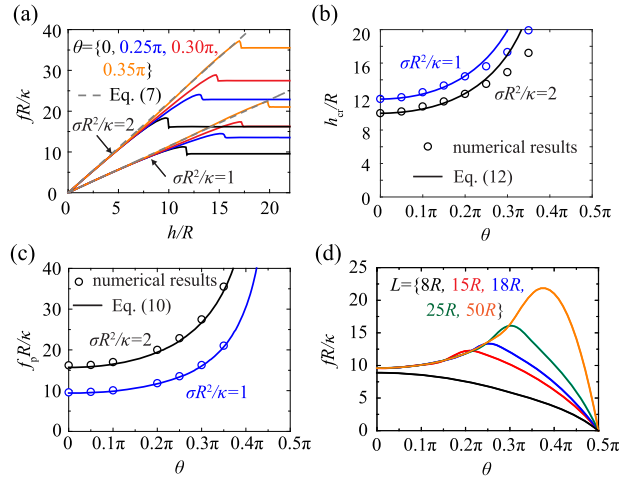

Fig. 5. System configurations at $h = 15R$, $\theta = 0.25\pi$ but different values of $\sigma R^2/\kappa$ (a). The protrusion phase diagram with respect to the protrusion angle θ and normalized membrane tension $\sigma R^2/\kappa$ at $h = 12R$, $15R$, and $18R$ (b).

Fig. 6. Resistive force at different values of the protrusion angle θ and the protrusion depth h/R. The normalized resistive force of the membrane as a function of h/R (a). The critical protrusion depth h_{cr} for the configurational transition as a function of θ (b). The plateau resistive force f_p versus θ (c). The resistive force as a function of θ for different tube lengths (d).

demonstrate that the outer membrane segment near the tube–membrane contact region undergoes a narrowing response as the resistive force approaches the peak value (Tian et al., 2018; Zhang et al., 2022). This localized constriction, made possible by the cylindrical shape of the tube, leads to a deceleration in the rate of the resistive force increase and eventually results in a slight drop, connecting to the plateau region of the resistive force. In contrast, a monotonically increasing force–indentation depth relationship is observed in the indentation of pore-spanning lipid membranes by parabolic indenters (Zhang et al., 2022). This is because the parabolic shape of the indenter does not allow for localized membrane constriction near the indenter–membrane contact region.

Increasing the protrusion angle θ or membrane tension σ leads to an increasing f_{max} and plateau resistive force f_p (Fig. 6a). Moreover, as θ increases, the configurational transition featured with the sudden force drop is delayed to a larger protrusion depth and the resistive force peak becomes higher, suggesting that perpendicular protrusion is stabilized by penalizing inclined protrusion with larger resistive force. A larger membrane tension prohibits the tube protrusion with a larger resistive force but favors the configurational transition at a smaller critical protrusion depth h_{cr} (Fig. 6b). The latter observation is consistent with Fig. 2c which indicates that the finial-roof configuration after the transition saves the membrane area in comparison with the tip-roof configuration.

3.6. Analytical prediction on the membrane resistive force

Fig. 6a shows that the force–protrusion depth relation can be approximated as a linear relation in the early protrusion stage followed by a force plateau stage. The curve slope at small h/R and the plateau force at large h/R are two feature factors of the force–protrusion depth relation. As shown in Fig. 6a, in the early protrusion stage the resistive force is almost linearly proportional to the protrusion depth, regardless to the value of the protrusion angle. Therefore, the curve slope at small h/R with an arbitrary θ can be obtained from the special case of $\theta = 0$.

At zero protrusion angle, the system adopts an axisymmetric configuration which can be described in a cylindrical coordinate system, and analytical solutions of the force–protrusion depth relation and membrane profile can be obtained based on the force balance along the z-axis and small membrane deformation assumption (Müller et al., 2007; Tang et al., 2019). In the current case of a very small ratio between the tube radius R and membrane radius ρ_{mem} (e.g., $R/\rho_{mem} = 0.002$ here), expressions of the force–depth relation and membrane profile at $\theta = 0$ in Tang et al. (2019) reduce to

$$f = \frac{2\pi\bar{\sigma}}{\eta(R)} \frac{h}{R} \frac{\kappa}{R}, \quad z = \frac{\eta(r)}{\eta(R)}h, \quad \eta(r) = \ln\frac{\rho_{mem}}{r} - \frac{K_0(\sqrt{\bar{\sigma}}\,r/R)}{\sqrt{\bar{\sigma}}K_1(\sqrt{\bar{\sigma}})}, \quad \bar{\sigma} = \frac{\sigma R^2}{\kappa}, \tag{7}$$

where $K_0(\alpha)$ and $K_1(\alpha)$ are the zeroth and first order of the second kind modified Bessel functions of α, respectively, and $r = (x^2 + y^2)^{1/2}$ is the radial distance. The $f - h/R$ relation in Eq. (7) agrees well with the numerical solutions (Fig. 6a). As the slope of the force–depth relation is insensitive to the protrusion angle (Fig. 6a), the $f - h/R$ relation in Eq. (7) can also be used to predict the early protrusion at $\theta \neq 0$.

Next, we seek an analytical prediction on the plateau force. As mentioned in the Section 3.3, for a free cylindrical membrane tubule of bending rigidity κ and tension σ, it has an equilibrium radius $r_0 = \sqrt{\kappa/(2\sigma)}$. Its corresponding elastic energy is $E_{el} = 4\pi r_0 \sigma L_{tube}$ with L_{tube} as the tube length (Derényi et al., 2002; Powers et al., 2002; Harmandaris and Deserno, 2006; Tian et al., 2018; Tang et al., 2019). Therefore, a pulling force maintaining the tubule configuration at L_{tube} and r_0 is

$$f = \partial E_{el} \big/ \partial L_{tube} = 2\pi\sqrt{2\sigma\kappa} \tag{8}$$

In the case of a rigid tube of radius R in a membrane tubule, at $R > r_0$ the membrane tubule is expanded to a configuration with radius R and forms tight sidewall contact with the enclosed tube. Thus, the elastic energy of the membrane tubule of length L_{tube} is $E_{\text{el}} = (2\pi R\sigma + \pi\kappa/R)L_{\text{tube}}$ and the corresponding pulling force required for the configuration maintenance is

$$f = \frac{\partial E_{\text{el}}}{\partial L_{\text{tube}}} = \frac{\pi\kappa}{R}\left(1 + \frac{2\sigma R^2}{\kappa}\right) \tag{9}$$

In the case of the tube protruding against the cell membrane at the protrusion angle θ (Fig. 6a), a protrusion depth increment Δh leads to a length increment $\Delta h/\cos\theta$ of the tubular membrane protrusion and an elastic energy increment $\Delta E_{\text{el}} = (2\pi R\sigma + \pi\kappa/R)\Delta h / \cos\theta$ with a physical approximation that the outer region of the membrane maintains its shape in the stage of resistive force saturation, as demonstrated in Fig. 2e and f. Therefore, the plateau of the resistive force f_{p} is

$$f_{\text{p}} = \frac{\Delta E_{\text{el}}}{\Delta h} = \frac{\pi\kappa}{R\cos\theta}\left(1 + \frac{2\sigma R^2}{\kappa}\right) \tag{10}$$

Eq. (10) agrees well with the numerical results (Fig. 6c). By equating the plateau force Eq. (10) with the linear force–depth relation Eq. (7), we can obtain a protrusion depth h',

$$h' = \frac{1 + 2\bar{\sigma}}{2\bar{\sigma}} \times \frac{\eta(R)}{\cos\theta} \text{ with } \eta(R) = \ln\frac{\rho_{\text{mem}}}{R} - \frac{K_0(\sqrt{\bar{\sigma}})}{\sqrt{\bar{\sigma}}K_1(\sqrt{\bar{\sigma}})} \tag{11}$$

Due to the oscillation of the resistance, the critical protrusion depth h_{cr} for the configurational transition is larger than h', which is approximated by multiplying h' with a constant factor α ($\alpha > 1$) as

$$h_{\text{cr}} = \alpha h'. \tag{12}$$

The scaling factor α is estimated by the case at $\theta = 0$, that is, $\alpha = h_{\text{cr}}^*(\theta = 0)/h'(\theta = 0)$. Here $h_{\text{cr}}^*(\theta)$ represents the numerical result of the critical protrusion depth. The scaling factor is calculated to be $\alpha = 1.41$ for $\sigma R^2/\kappa = 1$ and $\alpha = 1.56$ for $\sigma R^2/\kappa = 2$. As shown in Fig. 6b, the critical protrusion depth is well described by Eq. (12).

In the case of $\sigma R^2/\kappa < 1/2$, the tubular membrane protrusion has a radius of r_0, larger than the radius R of the protruding rigid tube. As the boundary condition used in the derivation of Eq. (7) is based on the tube radius R, the expression of Eq. (7) remains unaltered at any arbitrary value of $\sigma R^2/\kappa$. Eqs. (9)–(12) are based on the membrane tubule radius. By replacing the tube radius R with r_0, Eqs. (9)–(12) retain their validity in the case of $r_0 > R$, as demonstrated in Fig. S6 on the protrusion at $\sigma R^2/\kappa = 0.3$.

4. Discussion

4.1. Filopodia grow perpendicularly from the membrane edge

The membrane protrusion of the angle-dependent elastic deformation and resistive force have significant implications in the field of cell biology. One important case is related to the initiation, growth, and function of filopodia. Filopodia protrude perpendicularly from the leading edge of lamellipodia in most cases. Actin filaments of the filopodia are rooted at and intimately interwoven with the actin network beneath cell membranes. Filopodia are found to be initiated by reorganizing the dendritic network of lamellipodial filaments in a process involving the filament elongation, association, and convergence (Svitkina et al., 2003; Vignjevic et al., 2006). An interesting phenomenon is that filaments in the lamellipodia are usually orientated at roughly $\pm 35°$ with respect to the membrane normal direction, whereas the filaments of the filopodia grow perpendicularly from the membrane edge (Maly and Borisy, 2001). From a mechanical perspective, a reason for the different filament orientations in the above cases might be as follows. The resistive force due to the membrane deformation is smaller when the filopodial filaments protrude from the cell membrane perpendicularly rather than at an inclined angle. Filaments in the lamellipodia, however, propel the leading edge of the membrane and pull the cells forward during cell migration in a sheet-like conformation, i.e., the tip-roof conformation in our simulations. Our study shows that the tip-roof conformation is preferred with an inclined protrusion angle (Fig. 5b), consistent with the fact that the filaments in the lamellipodium are inclined to the membrane normal direction. Since the filaments with inclined protrusion angle are subjected to an increased membrane resistive force, the filaments in lamellipodium are crosslinked to form a nearly orthogonal network to enhance the rigidity against bending and buckling. Note that the expansion velocity of the membrane edge vanishes when the filaments are parallel to the membrane ($\theta = \pi/2$), thus the protrusion angle of filaments shall be a result of balancing the expansion velocity and the maintenance of expansion shape.

Moreover, the primary function of filopodia is to explore the local environment of cells, and as part of this function, filopodia can undergo sweeping motion with their tips rotating around fixed bases (Zidovska and Sackmann, 2011; Leijnse et al., 2015). During the sweeping, the protrusion angle of the filopodia increases, and according to the present results, the resistive force exerted on the actin filaments in the filopodia increases. To model the rotation of a preformed filopodia, we calculate the resistive force of a tube with a constant protrusion length L measured from the root of protrusion, while varying the protrusion angle (Fig. 6d). The resistive force of the preformed filopodia with a finial-roof conformation (e.g., $L=15R$, $18R$, $25R$, and $50R$) first increases with the protrusion angle and

then decreases as the resistive force ceases when the filament is parallel to the membrane. The resistive force at $\theta = 0$ is a local minimum, which suggests perpendicular filopodia is stable when exploring the surrounding environment by rotating around the membrane normal. Also, the membrane resistive force exerted on filopodia increases as the protrusion angle increases. To avoid the bending and buckling of the filaments, the protrusion angle cannot be too large, which can explain why the filopodia can only rotate within a limited angle (Zidovska and Sackmann, 2011; Leijnse et al., 2015). In addition to the perpendicular configuration, the resistive force decreases with the protrusion angle when the tube is laying down to the membrane edge (Fig. 6d), consistent with experimental observations that the filopodia can fold laterally back into the lamellipodium and contribute to the generation of contractile bundles parallel to cell edges (Nemethova et al., 2008).

Another related cellular activity is the protrusion and invasion of the intracellular rod-shaped bacterial parasite *Listeria monocytogenes*. During spread the infecting *Listeria monocytogenes* protrude against the cell membrane at a small protrusion angle (Tilney and Portnoy, 1989), and a small resistive force from the membrane deformation applied on the infecting *Listeria* as our results indicate.

4.2. Cell membrane stabilizes the perpendicular protrusion of filaments and encapsulates long filaments simultaneously

Morphologies of pressurized vesicles packed with straight and biologically stiff nanofibers, such as carbon nanotubes and gold nanowires, evolve from an axisymmetric lemon- to cherry- or ϕ-like shape as the fiber length increases (Tsai and Koenderink, 2015; Zhu et al., 2016; Zou et al., 2018; Ni and Papoian, 2021; Shi et al., 2023). The lemon-shaped vesicle features two tip-roof configurations at two poles of the deformed vesicle, whereas the cherry-shaped vesicle possesses a finial-roof configuration at one pole and a tip-roof configuration at the opposite pole. For the ϕ-shaped vesicle, the finial-roof configurations are formed at two vesicle poles. The configurational transition from the tip-roof to finial-roof as the protrusion depth increases is consistent with our results. Specifically, in the cherry-shaped vesicle, the equilibrium of the filament requires the force balance between filament ends with the tip-roof and finial-roof configurations. The force–depth relations in Fig. 6a suggest a spring-softening behavior with a drop of the resistive force accompanied by the transition from the tip-roof to finial-roof configuration. This nonmonotonic force–depth behavior indicates that the tip-roof and finial-roof configurations could suffer the same value of the resistive force, explaining the coexistence of two distinct configurations in the cherry-shaped vesicles.

For flexible filaments that can bend, buckle and coil upon constraints of vesicles, the filament ends either align at the periphery of the vesicle or cause shallow or tubular membrane protrusion locally perpendicular to the vesicle membrane (Tsai and Koenderink, 2015; Colin et al., 2020; Ni and Papoian, 2021; Shi et al., 2023), in accord with the two local minima of the protrusion force (Fig. 6d). Moreover, as a direct consequence of a larger membrane resistive force with the inclined protrusion, the flexible filaments bend and buckle as they approach the membrane with an inclination angle even in the case of low membrane rigidity, resulting in toroidal or disordered crumpled structures (Ni and Papoian, 2021; Shi et al., 2023). The bending and buckling of flexible filaments with an inclination angle enable the packing of very long filaments while maintaining the shape and integrity of cells, pivotal for cellular functions. For example, the gland thread cells of hagfish could encapsulate highly condensed filaments with length up to 10 cm (Fernholm, 1981). Engulfed long filamentous bacteria become supercoiled within macrophages (Prashar et al., 2013).

Taken together, the mechanical interplay between cell membranes and filaments leads to two different organization modes of encapsulated filaments. For the filaments requiring protrusion to achieve specific biological functions, the cell membrane stabilize the perpendicular protrusion by penalizing the inclined protrusion with higher membrane deformation energy and larger resistive force. Bending and bucking deformation are avoided by the rigidification of filaments via bundling or cross-linking. In contrast, the flexible filaments that need to be stored intracellularly either approach the membrane along an inclined direction or become tilted due to the bending and buckling deformation of perpendicular protrusion. The large resistive force of inclined protrusion further facilitates the bending and buckling of filaments, resulting in the coiling of filaments. The deformation of the cell membranes either stabilizing the perpendicular protrusion or forcing the transverse bending and buckling of filaments, which respectively enables the formation of filopodia or packing of long filaments in cells. In a more general perspective, the stabilized perpendicular protrusion and buckling of inclined protrusion indicate the role of membrane elastic deformation in modulating the packing mode of encapsulated filaments. The elastic deformation of cell membranes has been shown to play an essential role in growth of filopodia by inducing the bundling of actin filaments in filopodia (Liu et al., 2008). Here, our results suggest that the elastic deformation of cell membranes stabilize the perpendicular protrusion of stiff filaments by penalizing the inclined protrusion with higher membrane deformation energy and resistive force, revealing an uncovered role of the membrane deformation in filopodia growth.

4. Conclusions

Theoretical investigations on the angle-dependent interaction between a protruding tube and the cell membrane have been performed. System configurations at different values of protrusion angle and depth are determined. Two equilibrium configurations, the tip-roof and finial-roof configurations are identified. The configurational transition from the tip-roof to the finial-roof configuration is facilitated by decreasing the protrusion angle or increasing the membrane tension. Among configurations at different protrusion angles, any deviation from the perpendicular protrusion suffers a higher elastic deformation energy and a larger resistive force, suggesting the perpendicular protrusion is stabilized by the membrane deformation. Analytical estimations on the force–depth relation and membrane profile are provided. Specifically, the elastic deformation of the cell membrane is found to regulate the fate of encapsulated filaments by either stabilizing the perpendicular protrusion of stiff filaments or inducing the bending and buckling of flexible filaments, mechanisms underlying the formation of finger-like filopodia and the packing of flexible filaments in cells, respectively. Our results offer implications in analyzing filopodial orientation, invasion of the rod-shaped bacteria, instability of

confined filaments, and optimal design of nanowire arrays for cell property detection.

CRediT authorship contribution statement

Huayuan Tang: Methodology, Investigation, Validation, Writing – original draft, Writing – review & editing. **Hongfei Ye:** Methodology, Investigation, Validation, Writing – original draft, Writing – review & editing, Supervision, Funding acquisition. **Hongwu Zhang:** Methodology, Investigation, Validation, Writing – original draft, Writing – review & editing, Supervision, Funding acquisition. **Xin Yi:** Conceptualization, Methodology, Investigation, Validation, Formal analysis, Writing – review & editing, Supervision, Project administration, Funding acquisition. **Yonggang Zheng:** Conceptualization, Methodology, Investigation, Validation, Formal analysis, Writing – review & editing, Supervision, Project administration, Funding acquisition.

Declaration of Competing Interest

The authors declare that they have no known competing financial interests or personal relationships that could have appeared to influence the work reported in this paper.

Data availability

Data will be made available on request.

Acknowledgments

Supplementary materials

Supplementary material associated with this article can be found, in the online version, at doi:10.1016/j.jmps.2023.105500.

References

Atilgan, E., Wirtz, D., Sun, S.X., 2006. Mechanics and dynamics of actin-driven thin membrane protrusions. Biophys. J. 90, 65–76.

Brakke, K.A., 1992. The surface evolver. Exp. Math. 1, 141–165.

Chang, M., Lee, O.C., Bu, G., Oh, J., Yunn, N.O., Ryu, S.H., Kwon, H.B., Kolomeisky, A.B., Shim, S.H., Doh, J., Jeon, J.H., Lee, J.B., 2022. Formation of cellular close-ended tunneling nanotubes through mechanical deformation. Sci. Adv. 8, eabj3995.

Colin, L., Chevallier, A., Tsugawa, S., Gacon, F., Godin, C., Viasnoff, V., Saunders, T.E., Hamant, O., 2020. Cortical tension overrides geometrical cues to orient microtubules in confined protoplasts. Proc. Natl. Acad. Sci. U. S. A. 117, 32731–32738.

Datar, A., Bornschlögl, T., Bassereau, P., Prost, J., Pullarkat, P.A., 2015. Dynamics of membrane tethers reveal novel aspects of cytoskeleton-membrane interactions in axons. Biophys. J. 108, 489–497.

Derényi, I., Jülicher, F., Prost, J., 2002. Formation and interaction of membrane tubes. Phys. Rev. Lett. 88, 238101.

Fernholm, B., 1981. Thread cells from the slime glands of hagfish (Myxinidae). Acta Zool. 62, 137–145.

Gonzalez-Rodriguez, D., Guillou, L., Cornat, F., Lafaurie-Janvore, J., Babataheri, A., de Langre, E., Barakat, A.I., Husson, J., 2016. Mechanical criterion for the rupture of a cell membrane under compression. Biophys. J. 111, 2711–2721.

Harmandaris, V.A., Deserno, M., 2006. A novel method for measuring the bending rigidity of model lipid membranes by simulating tethers. J. Chem. Phys. 125, 204905.

He, S., Ji, B., 2017. Mechanics of cell mechanosensing in protrusion and retraction of lamellipodium. ACS Biomater. Sci. Eng. 3, 2943–2953.

Helfrich, W., 1973. Elastic properties of lipid bilayers: Theory and possible experiments. Z. Naturforsch. C 28, 693–703.

Jacquemet, G., Hamidi, H., Ivaska, J., 2015. Filopodia in cell adhesion, 3D migration and cancer cell invasion. Curr. Opin. Cell Biol. 36, 23–31.

Jiang, H., 2012. Dynamic sorting of lipids and proteins in multicomponent membranes. Phys. Rev. Lett. 109, 198101.

Jiang, H., Powers, T.R., 2008. Curvature-driven lipid sorting in a membrane tubule. Phys. Rev. Lett. 101, 018103.

Keber, F.C., Loiseau, E., Sanchez, T., DeCamp, S.J., Giomi, L., Bowick, M.J., Marchetti, M.C., Dogic, Z., Bausch, A.R., 2014. Topology and dynamics of active nematic vesicles. Science 345, 1135–1139.

Koster, G., Cacciuto, A., Derényi, I., Frenkel, D., Dogterom, M., 2005. Force barriers for membrane tube formation. Phys. Rev. Lett. 94, 068101.

Leijnse, N., Oddershede, L.B., Bendix, P.M., 2015. An updated look at actin dynamics in filopodia: Updated look at actin dynamics in filopodia. Cytoskeleton 72, 71–79.

Liu, A.P., Richmond, D.L., Maibaum, L., Pronk, S., Geissler, P.L., Fletcher, D.A., 2008. Membrane-induced bundling of actin filaments. Nat. Phys. 4, 789–793.

Maly, I.V., Borisy, G.G., 2001. Self-organization of a propulsive actin network as an evolutionary process. Proc. Natl. Acad. Sci. U. S. A. 98, 11324–11329.

Mattila, P.K., Lappalainen, P., 2008. Filopodia: molecular architecture and cellular functions. Nat. Rev. Mol. Cell Biol. 9, 446–454.

Mogilner, A., Rubinstein, B., 2005. The physics of filopodial protrusion. Biophys. J. 89, 782–795.

Müller, M.M., Deserno, M., Guven, J., 2007. Balancing torques in membrane-mediated interactions: exact results and numerical illustrations. Phys. Rev. E 76, 011921.

Nemethova, M., Auinger, S., Small, J.V., 2008. Building the actin cytoskeleton: filopodia contribute to the construction of contractile bundles in the lamella. J. Cell Biol. 180, 1233–1244.

Ni, H., Papoian, G.A., 2021. Membrane-MEDYAN: Simulating deformable vesicles containing complex cytoskeletal networks. J. Phys. Chem. B 125, 10710–10719.

Powers, T.R., Huber, G., Goldstein, R.E., 2002. Fluid-membrane tethers: minimal surfaces and elastic boundary layers. Phys. Rev. E 65, 041901.

Prashar, A., Bhatia, S., Gigliozzi, D., Martin, T., Duncan, C., Guyard, C., Terebiznik, M.R., 2013. Filamentous morphology of bacteria delays the timing of phagosome morphogenesis in macrophages. J. Cell Biol. 203, 1081–1097.

Raatz, M., Lipowsky, R., Weikl, T.R., 2014. Cooperative wrapping of nanoparticles by membrane tubes. Soft Matter 10, 3570–3577.

Raatz, M., Weikl, T.R., 2017. Membrane tubulation by elongated and patchy nanoparticles. Adv. Mater. Interfaces 4, 1600325.

Shi, C., Zou, G., Wu, Z., Wang, M., Zhang, X., Gao, H., Yi, X., 2023. Morphological transformations of vesicles with confined flexible filaments. Proc. Natl. Acad. Sci. U. S. A. 120, e2300380120.

Shi, X., von dem Bussche, A., Hurt, R.H., Kane, A.B., Gao, H., 2011. Cell entry of one-dimensional nanomaterials occurs by tip recognition and rotation. Nat. Nanotechnol. 6, 714–719.

Svitkina, T.M., Bulanova, E.A., Chaga, O.Y., Vignjevic, D.M., Kojima, S.I., Vasiliev, J.M., Borisy, G.G., 2003. Mechanism of filopodia initiation by reorganization of a dendritic network. J. Cell Biol. 160, 409–421.

Tang, X., Wang, J., Yi, X., 2019. Force barrier for lipid sorting in the formation of membrane nanotubes. J. Appl. Mech. 86, 121002.

Tian, F., Yue, T., Dong, W., Yi, X., Zhang, X., 2018. Size-dependent formation of membrane nanotubes: continuum modeling and molecular dynamics simulations. Phys. Chem. Chem. Phys. 20, 3474–3483.

Tilney, L.G., Portnoy, D.A., 1989. Actin filaments and the growth, movement, and spread of the intracellular bacterial parasite, Listeria monocytogenes. J. Cell Biol. 109, 1597–1608.

Tsai, F.C., Koenderink, G.H., 2015. Shape control of lipid bilayer membranes by confined actin bundles. Soft Matter 11, 8834–8847.

Vignjevic, D., Kojima, S.I., Aratyn, Y., Danciu, O., Svitkina, T., Borisy, G.G., 2006. Role of fascin in filopodial protrusion. J. Cell Biol. 174, 863–875.

Wu, Z., Yi, X., 2020. Structures and mechanical behaviors of soft nanotubes confining adhesive single or multiple elastic nanoparticles. J. Mech. Phys. Solids 137, 103867.

Yi, X., Shi, X., Gao, H., 2014. A universal law for cell uptake of one-dimensional nanomaterials. Nano Lett. 14, 1049–1055.

Yue, T., Zhang, X., Huang, F., 2014. Molecular modeling of membrane tube pearling and the effect of nanoparticle adsorption. Phys. Chem. Chem. Phys. 16, 10799–10809.

Zhu, W., von dem Bussche, A., Yi, X., Qiu, Y., Wang, Z., Weston, P., Hurt, R.H., Kane, A.B., Gao, H., 2016. Nanomechanical mechanism for lipid bilayer damage induced by carbon nanotubes confined in intracellular vesicles. Proc. Natl. Acad. Sci. U. S. A. 113, 12374–12379.

Zhang, X., Shi, C., Wu, Z., Yi, X., 2022. Indentation of pore-spanning lipid membranes: Spring-stiffening or -softening responses and apparent stiffness prediction. Extrem. Mech. Lett. 57, 101917.

Zidovska, A., Sackmann, E., 2011. On the mechanical stabilization of filopodia. Biophys. J. 100, 1428–1437.

Zou, G., Yi, X., Zhu, W., Gao, H., 2018. Packing of flexible nanofibers in vesicles. Extrem. Mech. Lett. 19, 20–26.

# Angle-dependent protrusion of cell membranes

Huayuan Tang[1,2], Hongfei Ye[2], Hongwu Zhang[2], Xin Yi[3,*], and Yonggang Zheng[2,*]

[1] Department of Engineering Mechanics, Hohai University, Nanjing 210098, P. R. China

[2] International Research Center for Computational Mechanics, State Key Laboratory of Structural Analysis for Industrial Equipment, Department of Engineering Mechanics, Faculty of Vehicle Engineering and Mechanics, Dalian University of Technology, Dalian 116024, P. R. China

[3] State Key Laboratory for Turbulence and Complex Systems, Department of Mechanics and Engineering Science, College of Engineering, Peking University, Beijing 100871, P. R. China

[*] Corresponding authors. Emails: zhengyg@dlut.edu.cn (Y.Z.) and xyi@pku.edu.cn (X.Y.)
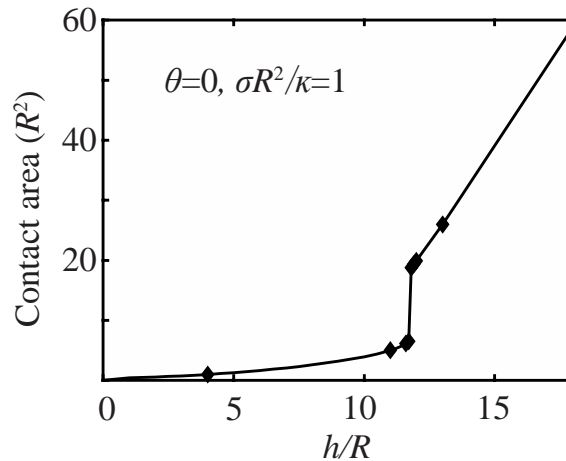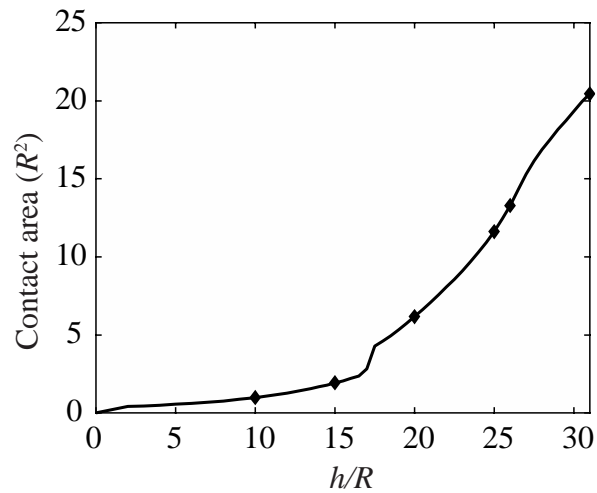
Fig. S1. Contact area between the membrane and tube as a function of the protrusion depth for the system with the protrusion angle $\theta = 0$ and membrane tension $\sigma R^2/\kappa = 1$. Representative conformations marked by diamond symbols here are shown in Fig. S2.
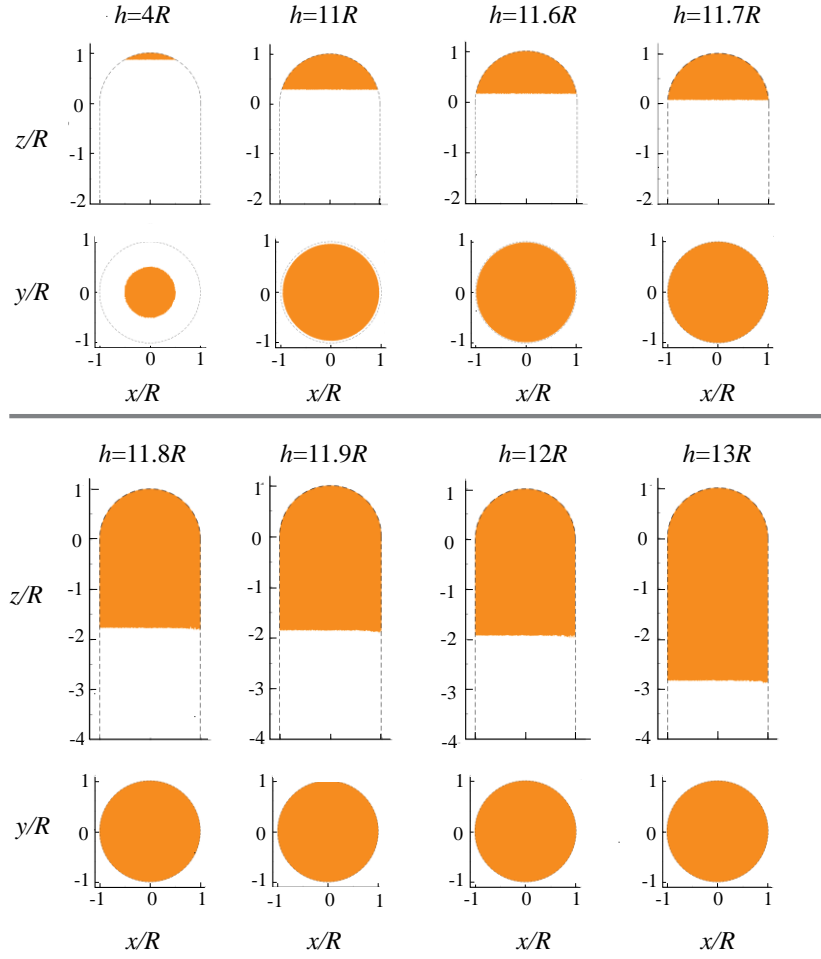
Fig. S2. Evolution of the contact region between the membrane and tube at various protrusion depths with the protrusion angle $\theta = 0$ and membrane tension $\sigma R^2/\kappa = 1$. The contact regions are shown in the x-z (up panels) and x-y (bottom panels) views. The contact regions are illustrated in orange and the tubes are shown in dashed lines with the coordination of the cap center set to be $(0, 0, 0)$ for comparison.
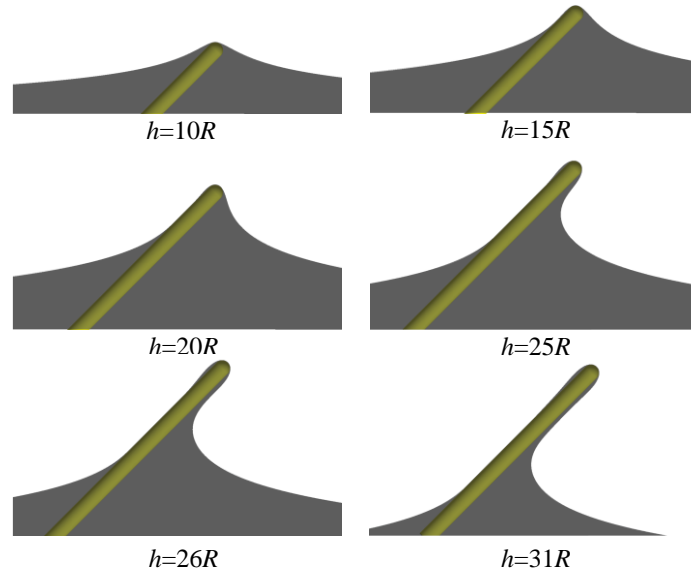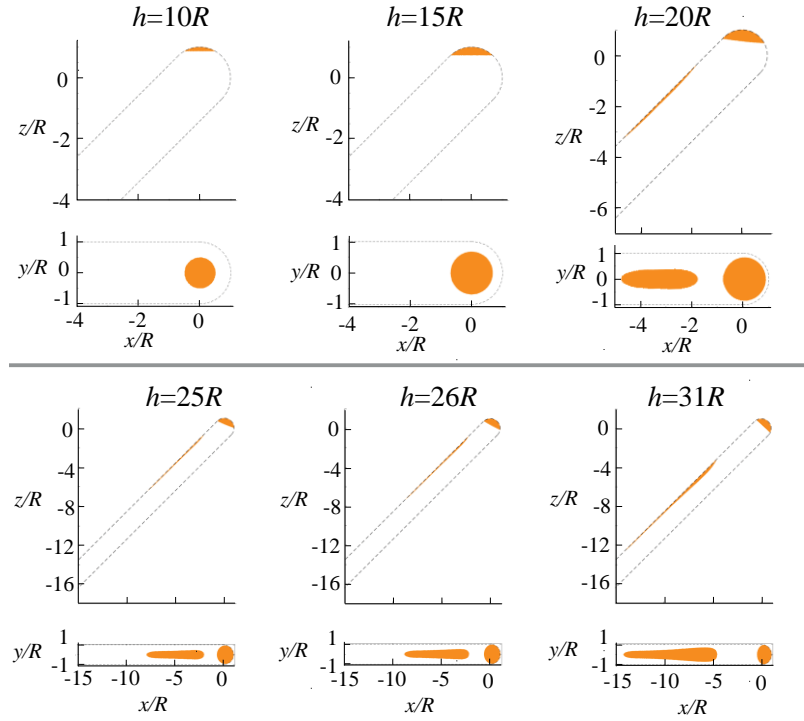
Fig. S3. Configurational evolution for the system of a small membrane tension $\sigma R^2/\kappa = 0.3$ with increasing protrusion depth h at the protrusion angle $\theta = 0.25\pi$.
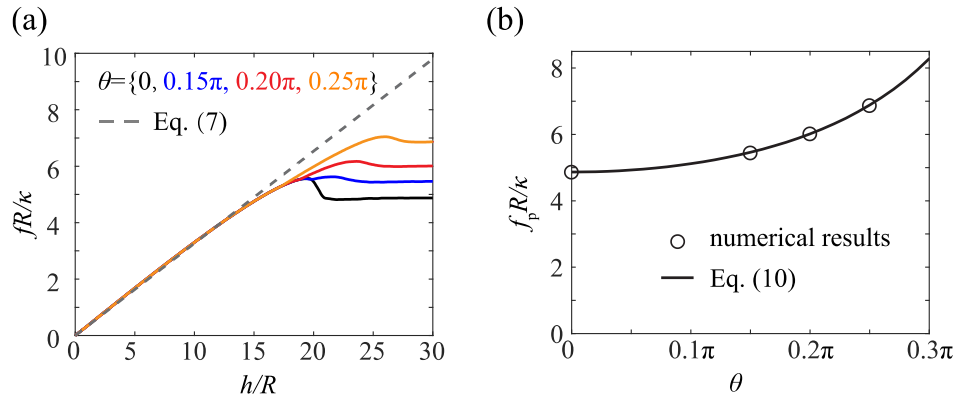

Fig. S4. Contact area between the membrane and tube versus the protrusion depth at $\theta = 0.25\pi$ and $\sigma R^2/\kappa = 0.3$.

Fig. S5. Evolution of the contact region at various protrusion depths with $\theta = 0.25\pi$ and $\sigma R^2/\kappa = 0.3$. The contact regions (orange) are shown in the x-z (upper panels) and x-y (lower panels) views with the Cartesian coordinate of the tube cap center set to be $(0, 0, 0)$.

Fig. S6. Protrusion of a tube against the cell membrane with $\sigma R^2/\kappa = 0.3$. The normalized resistive force of the membrane as a function of h/R (a). The plateau resistive force f_p versus θ (b). Analytical predictions in Eq. (7) and in Eq. (10) with R replaced by r_0 agree well with the numerical results.